



Effects of the fundamental oxide properties on the electric field-flash temperature during flash sintering

Rachman Chaim^{a,*}, Claude Estournès^b

^a Department of Materials Science and Engineering, Technion — Israel Institute of Technology, Haifa 32000, Israel

^b Université de Toulouse, CIRIMAT, CNRS INPT UPS, Université Paul-Sabatier, 118 route de Narbonne, F-31062 Toulouse cedex 9, France

ARTICLE INFO

Article history:

Received 10 December 2018

Accepted 16 January 2019

Available online xxxx

Keywords:

Flash sintering

Joule heating

Oxides

Crystal-type

Ionic potential

ABSTRACT

Flash sintering of oxide powders is associated with dissipated power in the narrow range $10\text{--}50\text{ W}\cdot\text{cm}^{-3}$ irrespective of their composition. By analysis and normalization of the experimental results from literature to constant particle size (100 nm) and applied electric field (500 V cm^{-1}), we show that the relative flash sintering temperature is dictated by the oxide crystal-type and its cation ionic potential resulting from its chemical composition. The expected flash onset temperature increases with the increase in fusion enthalpy and confirm the formation of liquid at the particle contacts as a mechanism for the powder densification.

© 2019 Acta Materialia Inc. Published by Elsevier Ltd. All rights reserved.

Flash sintering (FS) is a novel sintering method by which a simultaneous application of critical electric field and temperature leads to ultrafast densification of ceramic powder compacts within seconds. The process is often accompanied by a flash event hence termed flash sintering. The sudden increase in the electrical conductivity at the flash onset temperature leads to local Joule heating at the particle contacts. The different aspects of the powder characteristics and the process parameters were investigated during FS and different atomistic mechanisms, either in solid-state [1,2] or liquid-assisted [3], were proposed for the ultrafast densification. Nevertheless, the relation between the critical electric field and its flash temperature to the basic properties of the ceramic is still unknown. Compilation of flash sintering data of different oxides by Raj [4] revealed that the dissipated power at the flash event extends over a narrow range, $10\text{--}50\text{ W}\cdot\text{cm}^{-3}$. Raj and others showed that this power range is independent of the heating rate, the applied electric field [5], the specimen volume [6], and the powder particle size [7]. This narrow range of dissipated power in oxides with different chemical compositions and powder characteristics, may point to similar mechanisms activated at the flash onset conditions; consequently, some basic properties of the oxide should define its *relative* electric field-flash onset temperature.

In the present analysis, we follow our previous model [3,8] where the flash and the simultaneous abrupt increase in the electrical conductivity were related to the current percolation through the softened/melted particle contacts. Irrespective of the densification mechanism,

there is a common agreement that certain amount of power is needed to initiate the flash event. This arises from the current percolation threshold that necessitates softening/melting of critical volume fraction of the oxide at the particle contacts. The existence of the incubation time [9], where specimens with higher electric resistance (discs with identical diameters and increasing heights) exhibited shorter incubation times to the flash event at the isothermal conditions [7], confirms this trend. Therefore, as soon as the critical power for softening/melting of the particle contact is attained, the corresponding temperature acts as the flash temperature. Consequently, the relative flash temperature of a given oxide among all oxides should be dictated by its basic properties that define its crystal stability, i.e. fusion entropy, crystal structure, ionic potential, etc.

We used the data compiled by Raj [4] on different oxides flash sintered in air, in addition to oxides from other sources [10–24]. A few single data points were also included [10,14,15,19], and the appropriate oxide was underlined in Table I (see Supplement). We used and plotted these experimental FS data, where several different electric field - flash temperature combinations were available, as shown in Fig. 1. All these data were acquired in the same atmosphere (air), but vary in the heating rate, the range of the applied fields, as well as the flash temperatures and the original particle size. These plots often show linear to shallow hyperbolic relations between the flash temperature and the applied field on the semi-logarithmic scale (Fig. 1). In order to compare the flash sintering temperature data in Fig. 1, one should normalize the data with respect to the heating rate, particle size and the applied electric field.

It was shown that changing the heating rate from $2\text{ to }20\text{ }^{\circ}\text{C}\cdot\text{min}^{-1}$ during FS of $\text{Al}_2\text{O}_3/3\text{YSZ}$ composite yielded flash temperatures in the

* Corresponding author.

E-mail addresses: rchaim@technion.ac.il (R. Chaim), estourne@chimie.ups-tlse.fr (C. Estournès).

narrow temperature range, i.e. $\Delta T = 42^\circ\text{C}$, between 1165°C to 1207°C [4]. Therefore, we neglected the effect of the different heating rates among the various oxide candidates used for comparison in Table I (see Supplement). Nevertheless, we considered the effect of the particle size via the particle contact, and its electric resistance contribution to the overall specimen resistance [7]. Recently, a numerical model was developed to express the particle size effect on the flash sintering temperature associated with the particle contact resistance using 3YSZ (ZrO_2 stabilized with 3 mol% Y_2O_3 and exhibits tetragonal symmetry) as a model system [25]. The flash sintering temperature rapidly increased with the particle radius in the nanometer range, but tended to saturation at the micrometer particle size (Fig. 6 in ref. [25]). With respect to the previous model, we used the particle size of 100 nm subjected to electric field of $500\text{ V}\cdot\text{cm}^{-1}$ as a reference for comparing the flash sintering temperatures of the different oxides.

First, we selected flash temperatures of oxides that correspond to the applied field of $500\text{ V}\cdot\text{cm}^{-1}$, or the closest to this value. These temperatures were denoted as T_f in Table I (see Supplement). Second, we used the theoretical calculations of the particle size effect [25], and normalized the flash temperatures T_f of each oxide for 100 nm particle size (Fig. 6 in ref. [25], where 3YSZ with 100 nm particle size acts as a standard). This resulted in new flash sintering temperatures, denoted T_{f1} in Table I (see Supplement). Further, we assumed that the new estimated electric field–flash temperature curve, for a given oxide with 100 nm particles, will be parallel to its experimental curve and include T_{f1} . Finally, using this estimated curve, we selected the new flash temperature T_{f2} at the electric field of $500\text{ V}\cdot\text{cm}^{-1}$ (as listed in Table I in Supplement).

We plotted the resulting flash sintering temperatures normalized for the particle size of 100 nm and applied field of $500\text{ V}\cdot\text{cm}^{-1}$ versus oxide melting points in Fig. 2. Despite the limited data in Fig. 2, one can find some proximity between the data of groups of oxides with common crystal structure and composition stoichiometry. In this diagram, $\text{Ce}_{0.8}\text{Gd}_{0.2}\text{O}_{1.9}$, 8YSZ and 3YSZ resemble the CaF_2 crystal-type, where SnO_2 and TiO_2 resemble the Rutile crystal-type, and PbZrTiO_3 , BaTiO_3 , SrTiO_3 and KNbO_3 belong to the Perovskite crystal-type. Furthermore, MgTiO_3 and Al_2O_3 resemble similar crystal structures with some variations in ion occupancies. MgTiO_3 follow the Ilmenite crystal-type, which is a substitutional derivative of corundum (Al_2O_3) crystal-type, where the Mg and Ti fill the alternate basal plans. The connecting solid lines between the different oxides in Fig. 2 used only to highlight their crystal relations. Based on Fig. 2 it is clear that there is no direct relation between the flash temperatures to the melting points of the oxides. Nevertheless, the relative flash temperature depends on the

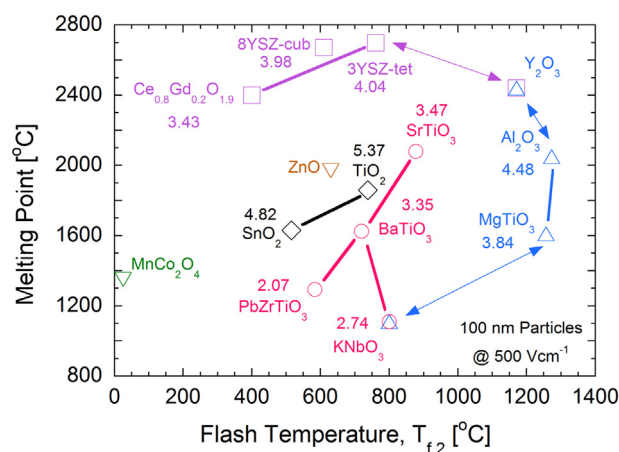


Fig. 2. Melting point–flash temperature diagram of oxides normalized for the 100 nm particle size under the $500\text{ V}\cdot\text{cm}^{-1}$ electric field. The numbers indicate the average ionic potential of the cations in the oxides. The lines used as guidelines only to highlight the oxides with similar crystal structure. The arrowed lines discussed in the text.

oxide crystal-type and stoichiometry as clearly is visible in Fig. 2. In this respect, Y_2O_3 is located between 3YSZ (tetragonal stabilized ZrO_2 with distorted CaF_2 -type structure) and Al_2O_3 (corundum). The Y_2O_3 with bixbyite BCC crystal structure is very close to $2 \times 2 \times 2$ supercell of CaF_2 , where one fourth of the oxygens are vacant per unit lattice compared to CaF_2 structure. Therefore, Y cations are six coordinated by the oxygen anions, as is true for Al cations in Al_2O_3 as the next neighbor to Y_2O_3 . Moreover, Y_2O_3 transforms at 2308°C to the CaF_2 structure prior to its melting [26]. The interrelation between bixbyite Y_2O_3 to the crystal-types of its neighbors, i.e. CaF_2 -type via lattice symmetry and Corundum via composition stoichiometry, symbolized by the two double arrowed lines. Similarly, LiNbO_3 (not treated in this paper) adopts the Ilmenite-type structure similar to MgTiO_3 , however, the Li and Nb are arranged in an ordered fashion within the basal plans of the pseudo-hexagonal lattice. Therefore, the larger K ion (0.152 nm) in KNbO_3 (in Fig. 2), compared to the smaller Li ion (0.088 nm) in LiNbO_3 , leads to the more stable perovskite-type structure than the Ilmenite-type structure. Consequently, KNbO_3 is also interrelated to both Perovskite-type and Ilmenite-type crystals as symbolized by the double arrowed line. The proximity between crystal-type and composition stoichiometry within each group of oxides and between the groups resemble the ‘structure–field maps’ of Goldschmidt followed by Roy and Muller [27].

In addition, moving from the bottom right to the top left of the diagram, the electric character of the oxides changes from the insulating dielectric, through the semiconducting (electronic)/ferroelectric and to the ionic conductors. Nevertheless, we expect that the present distribution of the various oxides in Fig. 2 dictated by the crystal stability against the application of the electric field. Formation of liquid at the particle contacts [8] must be associated with crystal instability, with disconnection of the interionic bonds. An important measure of the ion bond stability in the crystal subjected to the electric field is its ionic potential (IP), i.e. the cation charge (in our treatment) divided by its radius. In this regard, one should refer to the appropriate cation charge and its radius, dictated, respectively, by the crystal stoichiometry and its coordination number in the oxide crystal structure. We calculated the cationic potential for each oxide using the Shannon ionic radii [28]. The ionic potential for oxides with multiple cations was averaged over the IP of the different cations, considering their molar fractions in the oxide and taking into account the defect stoichiometry. We added the resulting ionic potentials near the oxide symbol in Fig. 2. Although the IP's vary in the narrow range, systematic increase in flash temperature with an increase in IP was observed for each crystal structure. Therefore, for an oxide with a given crystal-type, the average ionic potential seems

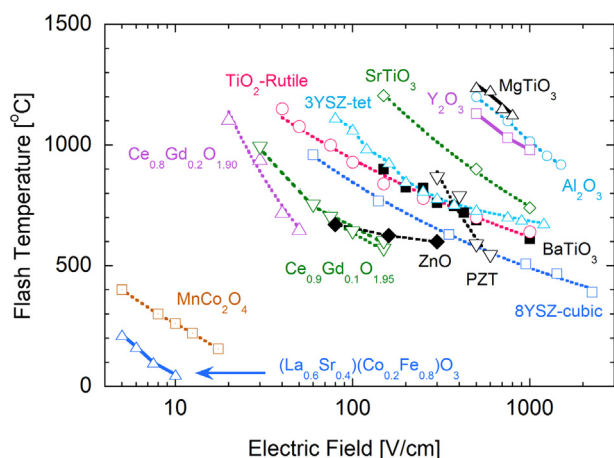


Fig. 1. Experimental flash temperature–electric field relations in different oxides: Al_2O_3 [1], BaTiO_3 [10], $\text{Ce}_{0.9}\text{Gd}_{0.1}\text{O}_{1.95}$ [11,12], $\text{Ce}_{0.8}\text{Gd}_{0.2}\text{O}_{1.90}$ [13], $(\text{La}_{0.6}\text{Sr}_{0.4})(\text{Co}_{0.2}\text{Fe}_{0.8})\text{O}_3$ [12], MgTiO_3 [16], MnCo_2O_4 [17], $\text{Pb}(\text{Zr}_{0.52}\text{Ti}_{0.48})\text{O}_3$ – PZT [18], SrTiO_3 [20], TiO_2 [21], Y_2O_3 [22], 3YSZ [23], 8YSZ [24], and ZnO [25].

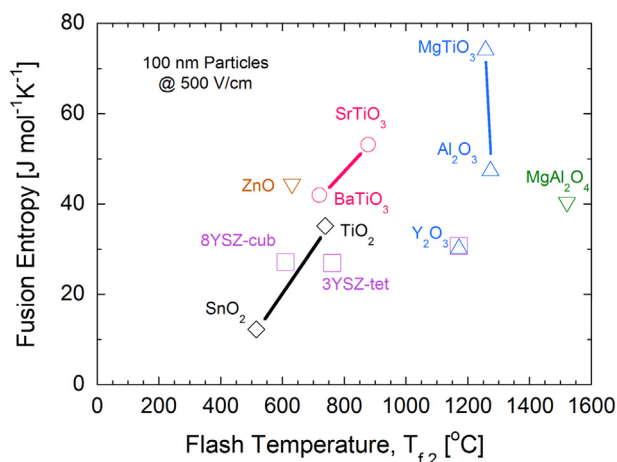


Fig. 3. Fusion entropy–flash temperature diagram of oxides normalized for the 100 nm particle size under the $500 \text{ V} \cdot \text{cm}^{-1}$ electric field. The lines used as guidelines only to highlight the oxides with similar crystal structure.

to be an appropriate fundamental material parameter that determines the relative flash temperature of the oxide.

Finally, we plotted the well-accepted fusion entropies of the flash sintered oxides, when available, versus the calculated flash temperature, T_{f2} as shown in Fig. 3. The flash temperature increases systematically with an increase in the fusion entropy, preserving the distribution pattern of the different crystal-types of oxides found in Fig. 2. The normalized flash temperature T_{f2} increases with increase in the fusion entropy. Compositional variation of the oxide by means of substitutional ions expected to increase the configurational disorder hence increase the solid entropy [29]. Consequently, smaller entropy change is expected during melting (i.e. fusion entropy) hence a decrease in the flash sintering temperature. These substitutional ions and point defects are expected to decrease the lattice stability towards melting, compared to its single cation pure oxide state. We calculated a significant decrease of the flash temperature (T_{f2}) down to room temperature, for multi-component CaF_2 -type [13], Perovskite-type [12], and Spinel-type [17] oxides (Table I – see Supplement). Flash at room temperature is not surprising by applying relatively high electric fields ($500 \text{ V} \cdot \text{cm}^{-1}$) to the defective oxides.

These findings on the relations between the relative flash temperature of a given oxide and its crystal-type and average ionic potential (Fig. 2), as well as its fusion entropy (Fig. 3) are powerful tools for predicting the expected flash temperature of all oxides. These findings strongly support the idea that flash onset temperature of the oxide dictated by local fusion of the particle contacts at the flash event. In this

regard, as was noted by Barsoum [30] the fusion entropy per atom/ion vary in a very narrow range around $\sim 10 \text{ J mol}^{-1} \text{ K}^{-1}$ regardless of the material composition, in agreement with the narrow range of the dissipated power observed at the flash onset temperature.

In summary, normalization of the flash sintering temperature data of various oxides to a reference condition of 100 nm particle size subjected to $500 \text{ V} \cdot \text{cm}^{-1}$ electric field revealed the primary task of the crystal structure, the ionic potential, and mainly the fusion entropy on the relative value of the flash temperature.

Supplementary data to this article can be found online at <https://doi.org/10.1016/j.scriptamat.2019.01.018>.

References

- [1] M. Cologna, J.S.C. Francis, R. Raj, *J. Am. Ceram. Soc.* 31 (2011) 2827–2837.
- [2] C. Schmerbauch, J. Gonzalez-Julian, R. Röder, C. Ronning, O. Guillon, *J. Am. Ceram. Soc.* 97 (2014) 1728–1735.
- [3] R. Chaim, *Materials* 10 (2017) 179.
- [4] R. Raj, *J. Am. Ceram. Soc.* 99 (2016) 3226–3232.
- [5] M. Cologna, B. Rashkova, R. Raj, *J. Am. Ceram. Soc.* 93 (2010) 3556–3559.
- [6] E. Bichaud, J.M. Chaix, C. Carry, M. Kleitz, M.C. Steil, *J. Eur. Ceram. Soc.* 35 (2015) 2587–2592.
- [7] J.S.C. Francis, M. Cologna, R. Raj, *J. Eur. Ceram. Soc.* 32 (2012) 3129–3136.
- [8] R. Chaim, C. Estournès, *J. Mater. Sci.* 53 (2018) 6378–6389.
- [9] M. Biesuz, P. Luchi, A. Quaranta, V.M. Sglavo, *J. Appl. Phys.* 120 (2016) 145107.
- [10] J.C. M'Peko, J.S.C. Francis, R. Raj, *J. Eur. Ceram. Soc.* 34 (2014) 3655–3660.
- [11] M. Biesuz, G. Dell'Agli, L. Spiridigliozzi, C. Ferone, V.M. Sglavo, *Ceram. Int.* 42 (2016) 11766–11771.
- [12] A. Gaur, V.M. Sglavo, *J. Am. Ceram. Soc.* 98 (2015) 1747–1752.
- [13] X. Hao, Y. Liu, Z. Wang, J. Qiao, K. Sun, *J. Power Sources* 210 (2012) 86–91.
- [14] N. Shomrat, S. Baltianski, C.A. Randall, Y. Tsur, *J. Eur. Ceram. Soc.* 35 (2015) 2209–2213.
- [15] H. Yoshida, P. Biswas, R. Johnson, M.K. Mohan, *J. Am. Ceram. Soc.* 100 (2017) 554–562.
- [16] X. Su, G. Bai, J. Zhang, J. Zhou, Y. Jia, *Appl. Surf. Sci.* 442 (2018) 12–19.
- [17] A. Gaur, V.M. Sglavo, *J. Eur. Ceram. Soc.* 34 (2014) 2391–2400.
- [18] X. Su, G. Bai, Y. Jia, Z. Wang, W. Wu, X. Yan, T. Ai, P. Zhao, *J. Eur. Ceram. Soc.* 38 (2018) 3489–3497.
- [19] R. Muccillo, E.N.S. Muccillo, *J. Eur. Ceram. Soc.* 34 (2014) 915–923.
- [20] A. Karakuscu, M. Cologna, D. Yarotski, J. Won, J.S.C. Francis, R. Raj, B.P. Uberuaga, *J. Am. Ceram. Soc.* 95 (2012) 2531–2536.
- [21] S.K. Jha, R. Raj, *J. Am. Ceram. Soc.* 97 (2014) 527–534.
- [22] H. Yoshida, Y. Sakka, T. Yamamoto, J.M. Lebrun, R. Raj, *J. Eur. Ceram. Soc.* 34 (2014) 991–1000.
- [23] R.I. Todd, E. Zapata-Solvas, R.S. Bonilla, T. Sneddon, P.R. Wilshaw, *J. Eur. Ceram. Soc.* 35 (2015) 1865–1877.
- [24] J.A. Downs, V.M. Sglavo, *J. Am. Ceram. Soc.* 96 (2013) 1342–1344.
- [25] R. Chaim, *J. Mater. Sci.* 53 (2018) 13853–13864.
- [26] A. Navrotsky, L. Benoist, H. Lefebvre, *J. Am. Ceram. Soc.* 88 (2005) 2942.
- [27] O. Muller, R. Roy, *The Major Ternary Structural Families*, Springer Verlag, Berlin, 1974.
- [28] R.D. Shannon, *Acta Crystallogr. A* 32 (1976) 751–767.
- [29] C.M. Rost, E. Sachet, T. Borman, A. Moballeghe, E.C. Dickey, D. Hou, J.L. Jones, S. Curtarolo, J.P. Maria, *Nat. Commun.* 6 (2015) 8485.
- [30] M. Barsoum, *Fundamentals of Ceramics*, McGraw-Hill, New York, 1997.